14th World Congress on Computational Mechanics (WCCM)
ECCOMAS Congress 2020)
Virtual Congress: 11-–15 January 2021
F. Chinesta, R. Abgrall, O. Allix and M. Kaliske (Eds)

A COMBINATION OF THE SCALED BOUNDARY FINITE ELEMENT METHOD WITH THE MORTAR METHOD

Jannis Bulling[1] **AND Hauke Gravenkamp**[2]

[1] Bundesanstalt für Materialforschung und -prüfung (BAM)
Unter den Eichen 87, 12205 Berlin, Germany
jannis.bulling@bam.de

[2] University of Duisburg-Essen
Universitätsstraße 15, 45141 Essen, Germany
hauke.gravenkamp@uni-due.de

Key words: Ultrasound, Scaled Boundary Finite Element Method, Mortar Method, Domain Decomposition

Abstract. Connecting different domains is one possibility to increase the performance of a numerical solution method. The Mortar Method is one of the well-established methods for this task. In this contribution, we focus on the solution of the elastodynamic wave equation by means of the scaled boundary finite element method and demonstrate that it is straightforward to connect different polygonal meshes by employing the Mortar Method in two dimensions. Examples show the stability for higher-order shape functions when performing h-refinement or p-refinement.

1 INTRODUCTION

The simulation of ultrasonic waves in a linearly elastic body can be computationally intensive. The reason is the relatively short wavelength compared to the body's dimensions at high frequencies. One possible approach to counteract the high computational costs is to decompose the domain into smaller parts. Each subdomain may be assigned its own efficient simulation method, and the subdomains can be solved in parallel. The Mortar Method is a well-established approach for coupling such subdomains [1, 2], allowing the combination of multiple solution methods within the same model. For elastodynamic waves, a few of many examples can be found in [3, 4, 5]. In the simplest case, different meshes can be connected.

In recent years, discretizations by polygonal elements have been of interest as they show the same flexibility as triangular elements for meshing while offering additional benefits. These benefits can be a smaller number of degrees of freedom to obtain the same accuracy. They also often show a better stability in case of distorted elements [6, 7]. Approaches to generating polygonal elements are the Voronoi Cell Finite Element Method [8], the Virtual Element Method [9] and finite element formulations based on the generalized barycentric coordinates [10, 11, 12], to name a few. The Virtual Element Method is based on shape functions which solve the differential equation, but are not directly computed; this leads to the name 'virtual.' The Voronoi Cell Finite Element Method, on the other hand, uses explicit stress functions to calculate the polygons' stiffness matrix.

Another approach to discretizing the emerging polygonal elements is the Scaled Boundary Finite Element Method [13, 14]. This semi-analytical method has many attractive properties, some of which are listed subsequently. A variety of material distributions, including anisotropic materials, can be considered. High-order shape functions can be used for optimal convergence properties [14, 15]. The approach treats singularities at crack tips and corners analytically [13, 16]. Especially in the frequency domain, the Scaled Boundary Finite Element Method reduces the approximation dimension because only degrees of freedom associated with the boundary of a polygonal element are required. Those desirable properties make the method particularly suitable for simulating the dynamic response in bodies with cracks, as is essential for many non-destructive testing and structural health monitoring applications [17, 18].

We present in this contribution a combination of the Scaled Boundary Finite Element Method with the Mortar Method in two dimensions. The second section gives a theoretical overview of both approaches. Subsequently, numerical examples demonstrate the stability of the combination for the polygonal boundary of the elements. The numerical models increase in complexity and are compared to results computed on non-divided domains by means of the Spectral Element Method (SEM) [15] .

2 Theory

This article considers the linear elastic wave equation on multiple subdomains. For the sake of simplicity, only two subdomains are used in the notation. The subdomains Ω_i, $i \in \{1,2\}$, are non-overlapping and have a common internal boundary Γ_{12}. In general, however, the approach can be extended to any number of subdomains. The strong form of the problem is

$$\partial_{tt}\mathbf{u} = \nabla \cdot \boldsymbol{\sigma}(\mathbf{u}), \qquad \mathbf{x} \in \Omega_i \qquad t \in [0,T] \tag{1}$$

$$\mathbf{n}\boldsymbol{\sigma} = \boldsymbol{\tau}, \qquad \mathbf{x} \in \Gamma \qquad t \in [0,T] \tag{2}$$

$$\mathbf{u}|_{\Omega_1} = \mathbf{u}|_{\Omega_2}, \qquad \mathbf{x} \in \Gamma_{12} \qquad t \in [0,T] \tag{3}$$

$$\mathbf{u} = \mathbf{0}, \qquad \mathbf{x} \in \Omega_i \qquad t = 0 \tag{4}$$

$$\partial_t \mathbf{u} = \mathbf{0}, \qquad \mathbf{x} \in \Omega_i \qquad t = 0 \tag{5}$$

with the linear stress $\boldsymbol{\sigma}$, the displacement $\mathbf{u}$, and a traction force $\boldsymbol{\tau}$ on the outer boundary Γ. Note the continuity condition on the internal boundary Γ_{12} in Equation (3). Figure 1 shows two polygonal meshes, which are coloured light and dark green indicating the subdomains. The common boundary is marked with a black line.

The Scaled Boundary Finite Element Method is deployed to approximate the linear elastic wave equation in each subdomain. For the approximation, the subdomains must be subdivided into polygons, which we call S-elements. In this article, the following approach is used to derive a polygonal mesh and its stiffness matrix:

- Start with a triangulation of the subdomain. For this paper, the triangulations are generated by 'gmsh' [19].
- Use the dual mesh of this triangulation to obtain a polygonal mesh. The dual mesh is constructed by defining each triangle's midpoints and connecting these midpoints of adjacent triangles. There are special steps to define the polygons next to the boundary. This approach is similar to [20].
- For each polygon, the local stiffness matrix is computed and assembled into the global stiffness matrix analogously to the Finite Element Method.

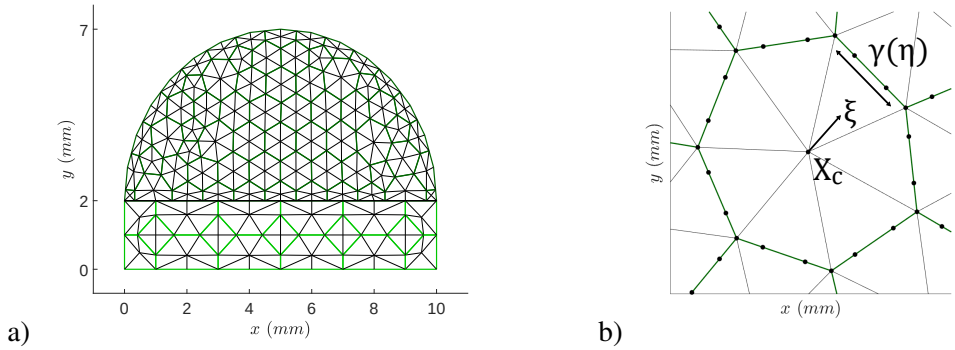

a) b)

Figure 1: a) Example mesh and b) Close up of a polygon

In the following paragraphs, we will summarize the crucial points for the derivation of the local stiffness matrices of each polygon.

The polygon's stiffness matrix is computed with the help of a particular coordinate system, called the scaled boundary coordinate system (see Figure 1b). Let $\boldsymbol{\gamma}(\eta)$ be a boundary parameterization given by straight line segments, where η is a local coordinate for each element. Choose a point $\mathbf{x}_c$ that "sees" the entire boundary. Then, the scaled boundary coordinates are defined as

$$\mathbf{x} = \xi(\boldsymbol{\gamma}(\eta) - \mathbf{x}_c) + \mathbf{x}_c, \tag{6}$$

where the point $\mathbf{x}_c$ is called the scaling center. Typically, the centroid is the scaling centre. In general, several types of shape functions and boundary parameterizations can be used [21], but, in this work, spectral shape functions of arbitrary degree p are used for the approximation of the displacement field and straight lines for the boundary of each polygon. Figure 2 shows the one-dimensional spectral shape functions $\mathbf{N}^{1d}$ for $\mathrm{p} = 3$. The vector-valued version is computed by $\mathbf{N} = \mathbf{N}^{1d} \otimes \mathbf{I}_2$, where $\otimes$ is the Kronecker tensor product, and $\mathbf{I}_2$ is the identity matrix of size two.

The SBFEM derivation starts with the weak form or principle of virtual work of Equations (1), (2) and (3) in the frequency domain, that is,

$$-\int \delta\mathbf{u} \cdot \omega^2 \mathbf{u} \, \mathrm{d}\Omega_i = -\int \nabla\delta\mathbf{u} \cdot \sigma(\mathbf{u}) \, \mathrm{d}\Omega_i + \int \delta\mathbf{u} \cdot \tau \, \mathrm{d}\Gamma + I_{12} \tag{7}$$

with the angular frequency ω. The term I_{12} enforces the continuity condition, but does not influence the derivation of the polygons and will be covered in Equation (22). The finite elements can be used to re-write the weak form in Equation (7) as an ordinary differential equation in the scaled boundary coordinate system, called the SBFEM-equation for the nodal displacement in a polygonal S-element:

$$\xi^2 \mathbf{E}_0 \partial_{\xi\xi}\mathbf{u}(\xi) + \xi(\mathbf{E}_0 + \mathbf{E}_1^\mathsf{T} - \mathbf{E}_1)\partial_\xi \mathbf{u}(\xi) - \mathbf{E}_2 \mathbf{u}(\xi) + \xi^2 \omega^2 \mathbf{M}_0 \mathbf{u}(\xi) = \mathbf{0}. \tag{8}$$

Note that $\mathbf{u}(\xi)$ is still a function of ξ. The matrices $\mathbf{E}_i$ are associated with the stress, and $\mathbf{M}_0$ is the boundary mass matrix,

$$\mathbf{M}_0 = \int \mathbf{N}(\eta)^\mathsf{T} \rho(\eta) \mathbf{N}(\eta) |j(\eta)| \, \mathrm{d}\eta, \qquad \mathbf{E}_0 = \int \mathbf{B}_1(\eta)^\mathsf{T} \mathcal{D}(\eta) \mathbf{B}_1(\eta) |j(\eta)| \, \mathrm{d}\eta, \tag{9}$$

$$\mathbf{E}_1 = \int \mathbf{B}_2(\eta)^\mathsf{T} \mathcal{D}(\eta) \mathbf{B}_1(\eta) |j(\eta)| \, \mathrm{d}\eta, \qquad \mathbf{E}_2 = \int \mathbf{B}_2(\eta)^\mathsf{T} \mathcal{D}(\eta) \mathbf{B}_2(\eta) |j(\eta)| \, \mathrm{d}\eta, \tag{10}$$

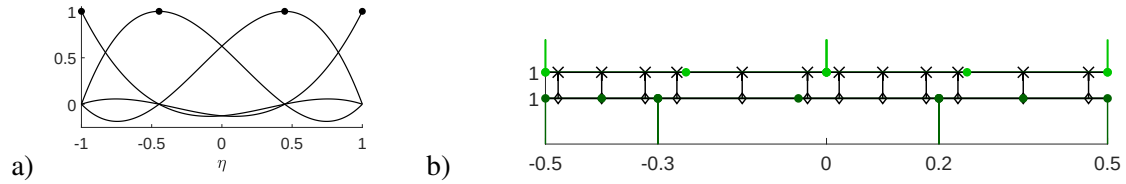

Figure 2: a) Spectral shape functions and b) Quadrature close up

where $\mathbf{B}_i$ are matrices that involve the shape functions and their derivatives with respect to η, $\mathcal{D}$ is the linear elastic tensor in Voigt notation, and $j(\eta)$ denotes the ξ-independent part of the Jacobi-determinant. Every column of these matrices corresponds to one shape function — similar to the FEM. A detailed derivation can be found in [13].

Assume that the inner nodal forces $\mathbf{q}$ can be expressed by a linear stiffness matrix $\mathbf{S}(\xi,\omega)$, i.e.,

$$\mathbf{q} = \left(\xi \mathbf{E}_0 \partial_\xi + \mathbf{E}_1^\mathsf{T}\right)\mathbf{u}(\xi) \tag{11}$$

$$= \mathbf{S}(\xi,\omega)\,\mathbf{u}(\xi). \tag{12}$$

Considerations regarding the scalability of the wave equation for linear elastic problems lead to the assumption that the stiffness matrix is a function of a single quantity $\chi = (\mathrm{i}\,\omega\xi)^2$, i.e., $\mathbf{S}(\xi,\omega) = \mathbf{S}(\chi)$. After a few transformations, one obtains the following matrix differential equation by considering an arbitrary displacement [14]

$$2\chi\partial_\chi\mathbf{S}(\chi) + (\mathbf{S}(\chi) - \mathbf{E}_1)\mathbf{E}_0^{-1}(\mathbf{S}(\chi) - \mathbf{E}_1^\mathsf{T}) - \mathbf{E}_2 - \chi\mathbf{M}_0 = \mathbf{0}. \tag{13}$$

This matrix differential system has no known analytical solution for $\omega > 0$, but Bazyar and Song published a rapidly converging iterative solution algorithm [13], which was later refined by Chen et al. [14]. The iterative solution algorithm is based on a matrix continued-fraction approach up to order M:

$$\mathbf{S}(\chi) = \mathbf{K} + \chi\mathbf{M} - \chi^2\mathbf{X}^{(1)}(\mathbf{S}^{(1)}(\chi))^{-1}(\mathbf{X}^{(1)})^\mathsf{T}, \tag{14}$$

$$\mathbf{S}^{(m)}(\chi) = \mathbf{S}_0^{(m)} + \chi\mathbf{S}_1^{(m)} - \chi^2\mathbf{X}^{(m+1)}(\mathbf{S}^{(m+1)}(\chi))^{-1}(\mathbf{X}^{(m+1)})^\mathsf{T}, \tag{15}$$

$$\mathbf{S}^{(M)}(\chi) = \mathbf{S}_0^{(M)} + \chi\mathbf{S}_1^{(M)}, \tag{16}$$

where $\mathbf{K}$, $\mathbf{M}$ are low-order approximations of the static stiffness and mass matrix, respectively. The construction of the higher-order matrices $\mathbf{S}_0^{(m)}$, $\mathbf{S}_1^{(m)}$, the pre-conditioner matrix $\mathbf{X}^{(m)}$, as well as $\mathbf{K}$, $\mathbf{M}$ can be found in [14]. At the boundary ($\xi = 1$), the inner nodal forces have to coincide with the nodal tractions $\mathbf{f}$, i.e.,

$$\mathbf{S}_\omega\mathbf{u} = \mathbf{f} \tag{17}$$

with $\mathbf{S}_\omega = \mathbf{S}(\chi)$, where Equations (14)-(16) are evaluated for $\chi = (\mathrm{i}\,\omega)^2$. Note that the size of $\mathbf{S}_\omega$ corresponds with the number of degrees on the boundary.

In the time domain, the continued-fraction approach can be resolved by introducing auxiliary variables for the displacement $\mathbf{u}^\mathsf{T} = ((\mathbf{u}^{(0)})^\mathsf{T},\dots,(\mathbf{u}^{(M)})^\mathsf{T})$, where each $\mathbf{u}^{(i)}$ is associated with one continued-fraction step. Equations (14)-(16) can be re-written and transferred to the time domain [13]

$$(\mathrm{i}\,\omega)^2\mathbf{M}_t\mathbf{u} = -\mathbf{K}_t\mathbf{u} + \mathbf{f}_t \rightsquigarrow \partial_{tt}\mathbf{M}_t\mathbf{u} = -\mathbf{K}_t\mathbf{u} + \mathbf{f}_t \tag{18}$$

with

$$\mathbf{M}_t = \begin{pmatrix} \mathbf{M} & -\mathbf{X}^{(1)} & \mathbf{0} & \cdots & \mathbf{0} \\ (-\mathbf{X}^{(1)})^\mathsf{T} & \mathbf{S}_1^{(1)} & -\mathbf{X}^{(2)} & \ddots & \vdots \\ \mathbf{0} & (-\mathbf{X}^{(2)})^\mathsf{T} & \ddots & \ddots & \mathbf{0} \\ \vdots & \ddots & \ddots & \ddots & -\mathbf{X}^{(M)} \\ \mathbf{0} & \cdots & \mathbf{0} & (-\mathbf{X}^{(M)})^\mathsf{T} & \mathbf{S}_1^{(M)} \end{pmatrix}, \qquad \mathbf{f}_t = \begin{pmatrix} \mathbf{f}^{(0)} \\ \mathbf{f}^{(1)} \\ \vdots \\ \vdots \\ \mathbf{f}^{(M)} \end{pmatrix}, \tag{19}$$

$$\mathbf{K}_t = \operatorname{diag}(\mathbf{K}, \mathbf{S}_0^{(1)}, \ldots, \mathbf{S}_0^{(M)}), \tag{20}$$

where $\mathbf{M}_t$ is the mass matrix, $\mathbf{K}_t$ is the static stiffness matrix, and $\mathbf{f}_t$ the time-dependent traction vector. The matrices $\mathbf{M}_t$, $\mathbf{K}_t$ are of size $n \times n$, where n is the number of degrees on the boundary times $M+1$. For the following investigations, we choose $M = \mathrm{p}$, where p is the polynomial degree of the shape functions. To solve Equation (18), many time-stepping methods can be employed. Here, the implicit Newmark-beta method with $\beta = 0.25$ and $\gamma = 0.5$ is used with the displacement as the primary variable, leading to the dynamic stiffness matrix

$$\mathbf{S}_t = \mathbf{K} + \frac{1}{\beta(\Delta t)^2}\mathbf{M}. \tag{21}$$

The continuity condition is enforced weakly in the Mortar Method. This is done by adding Lagrange multiplier terms (Equation (22)) in the weak form, see Equation (7).

$$I_{12} = \int (\delta\mathbf{u}|_{\Omega_1}(\mathbf{x}) - \delta\mathbf{u}|_{\Omega_2}(\mathcal{P}(\mathbf{x})))\boldsymbol{\lambda}(\mathbf{x})\,\mathrm{d}\Gamma_{12} + \int (\mathbf{u}|_{\Omega_1}(\mathbf{x}) - \mathbf{u}|_{\Omega_2}(\mathcal{P}(\mathbf{x})))\delta\boldsymbol{\lambda}(\mathbf{x})\,\mathrm{d}\Gamma_{12}. \tag{22}$$

The physical interpretation is that the Lagrange multipliers are additional variables representing traction forces between the subdomains. There are two finite element meshes on the common boundary for this formulation due to the two subdomains. One of these boundaries – often the finer mesh – is chosen as the non-mortar side, which can be alternatively termed 'master side.' The integration and definition of the Lagrange multipliers are applied on this non-mortar side. The displacement of the mortar/slave side is evaluated at the nearest point projection $\mathcal{P}$. For interpolating the Lagrange multipliers, spectral shape functions of the same degree as for the displacements are used in nearly all elements. The Lagrange multipliers are continuous on each internal boundary. The exceptions are elements adjacent to a cross-point, at which at least three subdomains intersect. See Figure 7a) for an example. The Lagrange multipliers are discontinuous across at this cross-point for all polynomial degrees. In general, the cross-point of a domain can be over-constrained by the Mortar Method [1, 23]. To counteract the over-constraining, a cross-point modification can be applied, for example, the polynomial degree of elements next to a cross-point can be lowered by one [1]. For linear shape functions, this leads to discontinuous, constant shape functions adjacent to a cross-point.

An exact integration is applied to reach higher-order convergence. The process is shown in Figure 2b), where both sides are separated by a small gap. The quadrature points of a 3-point Gaussian integration are marked by '$\diamondsuit$' on the non-mortar side and '$\times$' on the mortar side, respectively.

The final form of the global stiffness matrix constitutes a saddle point problem

$$\begin{pmatrix} \mathbf{S}_1 & \mathbf{0} & \mathbf{L}_1 \\ \mathbf{0} & \mathbf{S}_2 & \mathbf{L}_2 \\ \mathbf{L}_1^\mathsf{T} & \mathbf{L}_2^\mathsf{T} & \mathbf{0} \end{pmatrix} \begin{pmatrix} \mathbf{u}_1 \\ \mathbf{u}_2 \\ \boldsymbol{\lambda} \end{pmatrix} = \begin{pmatrix} \mathbf{f}_1 \\ \mathbf{f}_2 \\ \mathbf{0} \end{pmatrix}, \tag{23}$$

where $\mathbf{S}_i$ is the dynamic stiffness matrix of each subdomain – Equation (17) for the frequency domain and Equation (21) for the time domain. $\mathbf{L}_i$ are the matrices associated with Equation (22) coupling the Lagrange multiplier vector and the displacement of each subdomain.

The saddle point problem quite naturally leads to a parallelization process by considering the first step of a Uzawa-like-algorithm [22] which solves Equation (23) equivalently

$$\mathbf{S}_i \mathbf{y}_i = \mathbf{f}_i \qquad \forall i \in \{1,2\}, \tag{24}$$

$$\mathbf{C}\boldsymbol{\lambda} = \sum_i \mathbf{L}_i \mathbf{y}_i \qquad \mathbf{C} = \sum_i \mathbf{L}_i^\mathsf{T} \mathbf{S}_i \mathbf{L}_i, \tag{25}$$

$$\mathbf{S}_i \mathbf{u}_i = \mathbf{f}_i - \mathbf{L}_i \boldsymbol{\lambda} \qquad \forall i \in \{1,2\}, \tag{26}$$

where the first and last equation can be solved in parallel, and the second equation transfers information from one subdomain to the other. By the numerical examples in the next section, we show that the Schur complement matrix $\mathbf{C}$ is stable in the context of the SBFEM. In this preliminary study, a direct solver is applied to each matrix system. For the time domain, the Cholesky factorization is used as a pre-conditioner for $\mathbf{S}_i$ as well as the Schur complement matrix $\mathbf{C}$.

3 Numerical Examples

This section presents some numerical examples, starting with the simple case of a rectangle. A bell-shaped domain consisting of multiple subdomains is investigated as a second example.

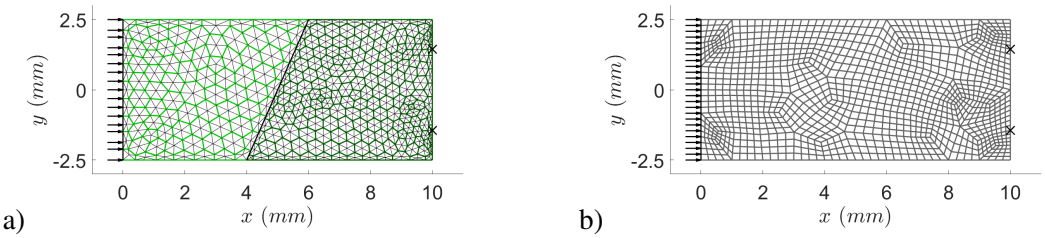

Figure 3: Problem overview for the rectangle: a) SBFEM-mesh b) Spectral element mesh

Figure 3a) shows a rectangular domain which is split into two subdomains with non-matching meshes. This domain is subject to a uniform normal traction on the left side. The traction is indicated by black arrows in the same figure. We will show results for the time and frequency domain, starting with the former. The traction varies in time as a Gaussian pulse with a center frequency f_0 of 1 MHz, i.e.,

$$\tau(t) = \sin(2\pi t f_0) \cdot \exp\left(-0.5(t - 0.25 f_0^{-1})^2 / (f_0^{-1})^2\right). \tag{27}$$

The material parameters are given in Table 1 and plane strain is assumed. The time step is chosen as $(100 f_0)^{-1}$ in the Newmark method. The SBFEM and the reference solution use the same Newmark method with the same time resolution, hence, the error will be dominated by the spatial discretization.

Figure 4a) shows the result of x-displacement at the upper black point marked in Figure 3a). The SBFEM-approximation is compared to a reference solution calculated by means of a very highly p-refined Spectral Element approximation (SEM) – also shown in Figure 4a). We observe a good agreement between both methods. For a deeper investigation, the error between the reference solution and the SBFEM is computed as follows

$$\text{error} = \sqrt{\sum_i \sum_j \left(u^h(P_j,t_i) - u^{\text{ref}}(P_j,t_i)\right)^2} \Big/ \sqrt{\sum_i \sum_j \left(u^{\text{ref}}(P_j,t_i)\right)^2}, \tag{28}$$

where P_i are the two Gaussian integration points on the right boundary (marked with black crosses). Figure 5 shows the error for h-refinement and p-refinement, respectively. The h-refinement is based

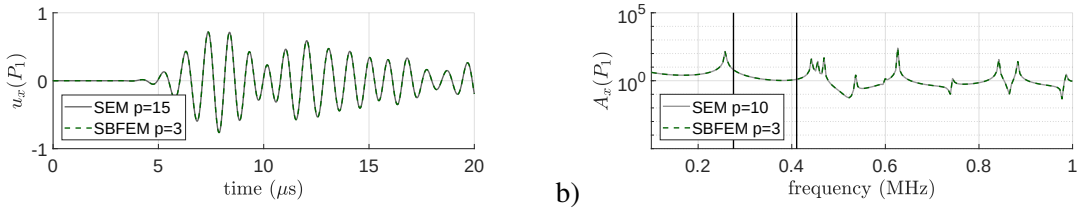

a) b)

Figure 4: Example displacements: a) time domain b) frequency domain for the rectangle (Figure 3)

on a new triangulation for each refinement step. For all figures, 'DoF' is an abbreviation for all the degrees of freedom, including the Lagrange multipliers if they exist. We do not report convergence rates since the plots are based on point-wise evaluation and use the total number of degrees of freedom. However, comparing the results to the Spectral Element Method on the undivided mesh (see Figure 3), we observe that the lines approach each other. The usual behaviour with steeper slopes for higher degree approximation and exponential convergence for p-refinement is visible. The SEM is known to achieve optimal rates of convergence, so Figure 5 indicates that the proposed SBFEM achieves the same rates on subdivided meshes. Note that this study only attempts to demonstrate the validity of the approach while an undivided mesh is more efficient for such a simple domain.

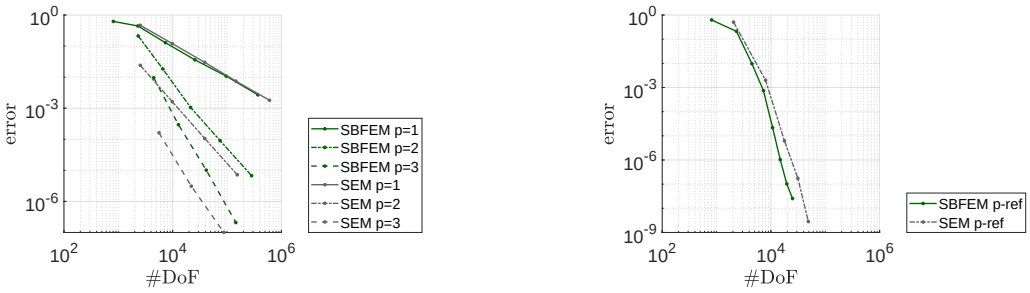

a) b)

Figure 5: Error time domain: a) h-refinement b) p-refinement for the rectangle (Figure 3)

For the simulation in the frequency domain, unit tractions for 200 frequencies uniformly spaced between 0 MHz and 1 MHz are used. Figure 4b) shows the results for the SBFEM on two subdomains and

the Spectral Element Method reference solution on the undivided domain. The error for both methods between the displacement evaluated at the same locations as in the time domain is summed in the range marked by the two black lines in Figure 4b). This range was chosen to avoid the resonance peaks where the numerical solution tends to be inaccurate. The error is shown in Figure 6 for h-and p-refinement. In the case of h-refinement, the same sequence of polygonal meshes is used as for the time domain. The number of degrees of freedom is much lower because only degrees on the boundary are required in the frequency domain.

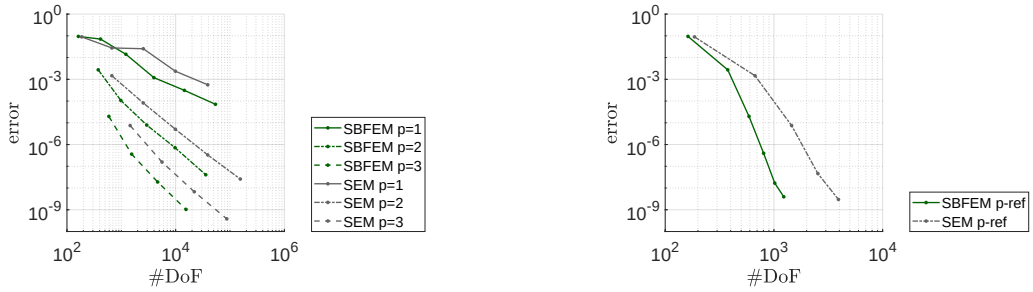

a) b)

Figure 6: Error frequency domain: a) h-refinement b) p-refinement for the rectangle (Figure 3)

The final example shows a subdivision of a bell-shaped domain into three parts. The structure is excited at the top surface. The same excitation as in the first example is used, but the center frequency f_0 is 2 MHz. The material properties and time stepping rule coincide with the first example. Figure 7 shows the error for h-refinement using the SBFEM (Subplot a)) and the Spectral Element Method (Subplot b)) at the points marked with black crosses. The cross-point modification mentioned in the previous section is applied. However, in out tests, the error with and without cross-point modification shows the same behaviour.

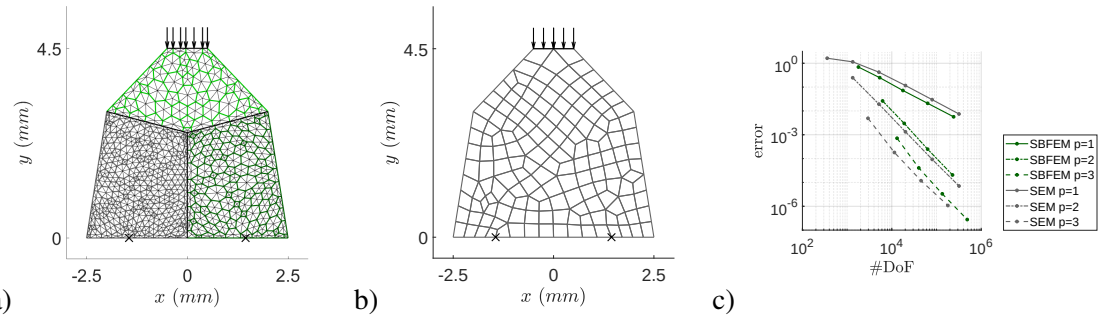

a) b) c)

Figure 7: Bell-shaped domain: a) SBFEM-mesh b) Spectral element mesh c) Error for h-refinement

4 Conclusions

The extension of the Scaled Boundary Finite Element Method by the Mortar Method and domain decomposition is straightforward. The formulation is stable for higher-order shape functions in both the

Table 1: Structural steel

Isotropic material							
E:	200	GPa	ν:	0.3	ρ:	7.85	$\mathrm{g\,cm^{-3}}$

time- and the frequency-domain. The usual convergence behavior is observed if the shape functions used for the displacement and the Lagrange multipliers are of the same degree (- except elements adjacent to a cross-point). A cross-point modification is applied to counteract an over-constraining of the approximation if several subdomains intersect. The results are improved by an exact quadrature for the interface. For these small-scale examples, no decrease in the computation time was achieved due to the parallelization.

Acknowledgements

The authors thankfully acknowledge financial support from the German Research Foundation (Deutsche Forschungsgemeinschaft (DFG) - project: 428590437).

REFERENCES

[1] Wohlmuth, B. I. "A mortar finite element method using dual spaces for the Lagrange multiplier." *SIAM Journal on Numerical Nnalysis* 38.3 (2000): 989-1012.

[2] Seshaiyer, P., and Manil S. "Convergence results for non-conforming hp methods: The mortar finite element method." *Contemporary Mathematics* 218 (1998): 453-459.

[3] Casadei, F., Gabellini, E., Fotia, G., Maggio, F., and Quarteroni, A. "A mortar spectral/finite element method for complex 2D and 3D elastodynamic problems." *Computer Methods in Applied Mechanics and Engineering* 191.45 (2002): 5119-5148.

[4] Imperiale, A., and Demaldent, E. "A macro-element strategy based upon spectral finite elements and mortar elements for transient wave propagation modeling. Application to ultrasonic testing of laminate composite materials." *International Journal for Numerical Methods in Engineering* 119.10 (2019): 964-990.

[5] Hauret, P., and Le Tallec, P. "A discontinuous stabilized mortar method for general 3d elastic problems." *Computer Methods in Applied Mechanics and Engineering* 196.49-52 (2007): 4881-4900.

[6] Mengolini, M., Matías F. B. and Alejandro M. A. "An engineering perspective to the virtual element method and its interplay with the standard finite element method." *Computer Methods in Applied Mechanics and Engineering* 350 (2019): 995-1023.

[7] Zhang, P., Du, C., Tian, X., and Jiang, S. "A scaled boundary finite element method for modelling crack face contact problems." *Computer Methods in Applied Mechanics and Engineering* 328 (2018): 431-451.

[8] Ghosh, S., and Mallett, R. L. "Voronoi cell finite elements." *Computers & Structures* 50.1 (1994): 33-46.

[9] Da Veiga, L. B., Brezzi, F., and Marini, L. D. "Virtual elements for linear elasticity problems." *SIAM Journal on Numerical Analysis* 51.2 (2013): 794-812.

[10] Floater, M. S., and Lai, M. J. "Polygonal spline spaces and the numerical solution of the Poisson equation." *SIAM Journal on Numerical Analysis* 54.2 (2016): 797-824.

[11] Sukumar, N., and Tabarraei, A. "Conforming polygonal finite elements." *International Journal for Numerical Methods in Engineering* 61.12 (2004): 2045-2066.

[12] Sukumar, N. "Quadratic maximum-entropy serendipity shape functions for arbitrary planar polygons." *Computer Methods in Applied Mechanics and Engineering* 263 (2013): 27-41.

[13] Bazyar, M. H., and Song, C. "A continued-fraction-based high-order transmitting boundary for wave propagation in unbounded domains of arbitrary geometry." *International Journal for Numerical Methods in Engineering* 74.2 (2008): 209-237.

[14] Chen, D., Birk, C., Song, C., and Du, C. "A high-order approach for modelling transient wave propagation problems using the scaled boundary finite element method." *International Journal for Numerical Methods in Engineering* 97.13 (2014): 937-959.

[15] Gravenkamp, H., and Natarajan, S. "Scaled boundary polygons for linear elastodynamics." *Computer Methods in Applied Mechanics and Engineering* 333 (2018): 238-256.

[16] Bulling, J., Gravenkamp, H., and Birk, C. "A high-order finite element technique with automatic treatment of stress singularities by semi-analytical enrichment." *Computer Methods in Applied Mechanics and Engineering* 355 (2019): 135-156.

[17] Gravenkamp, H. "Efficient simulation of elastic guided waves interacting with notches, adhesive joints, delaminations and inclined edges in plate structures." *Ultrasonics* 82 (2018): 101-113.

[18] Lugovtsova, Y., Bulling, J., Boller, C., and Prager, J. "Analysis of guided wave propagation in a multi-layered structure in view of structural health monitoring." *Applied Sciences* 9.21 (2019): 4600.

[19] Geuzaine, C., and Remacle, J. F. "Gmsh: A 3-D finite element mesh generator with built-in pre- and post-processing facilities." *International Journal for Numerical Methods in Engineering* 79.11 (2009): 1309-1331.

[20] Ooi, E. T., Song, C., Tin-Loi, F., and Yang, Z. "Polygon scaled boundary finite elements for crack propagation modelling." *International Journal for Numerical Methods in Engineering* 91.3 (2012): 319-342.

[21] Gravenkamp, H., Saputra, A. A., and Duczek, S. "High-order shape functions in the scaled boundary finite element method revisited." *Archives of Computational Methods in Engineering* (2019): 1-22.

[22] Bramble, J. H., Pasciak, J. E., and Vassilev, A. T. "Analysis of the inexact Uzawa algorithm for saddle point problems." *SIAM Journal on Numerical Analysis* 34.3 (1997): 1072-1092.

[23] Brivadis, E., Buffa, A., Wohlmuth, B., and Wunderlich, L. "Isogeometric mortar methods." *Computer Methods in Applied Mechanics and Engineering* 284 (2015): 292-319.